A CO_2-Stable Hollow-Fiber Membrane with High Hydrogen Permeation Flux

Yan Chen, Qing Liao, Zhong Li, and Haihui Wang
School of Chemistry and Chemical Engineering, South China University of Technology, Wushan Road 381, Guangzhou, China

Yanying Wei, Armin Feldhoff, and Jürgen Caro
Institute of Physical Chemistry and Electrochemistry, Leibniz University of Hannover, Callinstrasse 3A, 30167 Hannover, Germany

DOI 10.1002/aic.14772
Published online March 11, 2015 in Wiley Online Library (wileyonlinelibrary.com)

A Mo-substituted lanthanum tungstate mixed proton-electron conductor, $La_{5.5}W_{0.6}Mo_{0.4}O_{11.25-\delta}$ (LWM04), was synthesized using solid state reactions. Dense U-shaped LWM04 hollow-fiber membranes were successfully prepared using wet-spinning phase-inversion and sintering. The stability of LWM04 in a CO_2-containing atmosphere and the permeation of hydrogen through the LWM04 hollow-fiber membrane were investigated in detail. A high hydrogen permeation flux of 1.36 mL/min cm^2 was obtained for the U-shaped LWM04 hollow-fiber membranes at 975°C when a mixture of 80% H_2−20% He was used as the feed gas and the sweep side was humidified. Moreover, the hydrogen permeation flux did not significantly decrease over 70 h of operation when fed with a mixture containing 25% CO_2, 50% H_2, and 25% He, indicating that the LWM04 hollow-fiber membrane has good stability under a CO_2-containing atmosphere. *AIChE J*, 61: 1997–2007, 2015
Keywords: membrane, hollow-fiber, H_2, mixed conductor, permeation

Introduction

Hydrogen is gaining more attention because it is generally regarded as an important fuel of the future.[1,2] The widespread use of H_2 as an energy source could help alleviate concerns regarding energy security, global climate change, and air quality. The most important source for H_2 is steam reforming of natural gas followed by the water-gas shift reaction and separation steps. New technologies for the inexpensive and effective separation of H_2 are in high demand because traditional H_2 separation technologies require high capital costs and lead to significant energy losses. Supported Pd and Pd alloy (23% Ag) membranes allow the highly selective separation of H_2 at temperatures of 300–500°C.[3,4] However, thin Pd and Pd alloy membranes are brittle. In the presence of hydrocarbons, carbides are formed and incorporated in the grain boundaries of the Pd-layer, and the membrane is subsequently destroyed. Moreover, H_2S and CO poisoning must be considered. These disadvantages prevent the widespread application of Pd and Pd alloy membranes in the H_2 separation industry. Although narrow pore zeolite membranes could separate H_2 (having a kinetic diameter of 0.29 nm), zeolite membranes have not been commercialized. The only zeolite membrane with a proven size-selectivity for industrial gas separation applications is the zeolite-type mobil fifth (MFI) with a 0.55-nm pore width.[5,6] However, only a low separation factor of 70 could be obtained for H_2/*i*-butane separation at 500°C. As an alternative, dense mixed proton-electron conducting ceramic membranes can be used for a simple and cost-effective process. This novel membrane type can selectively permeate H_2 at high temperatures, and the membrane separation process does not require an additional external electrical circuit due to its inherent mixed conductivity. This type of membrane has great potential for H_2 purification because it offers several advantages over alternative technologies, including lower energy consumption, lower materials cost, simpler operation, and the use of equipment that is more compact.

Currently, perovskite-type oxides are the most commonly studied mixed proton-electron conducting ceramic materials, particularly doped $SrCeO_3$ and $BaCeO_3$ materials.[7,8] However, the H_2 permeation fluxes of these types of ceramic membranes are too low to meet industrial standards. For example, Song et al.[9] investigated the H_2 permeability of a $SrCe_{1-x}M_xO_{3-\delta}$ ($x = 0.05$, M = Eu, Sm) membrane and found that the H_2 permeation flux was approximately 0.0035 mL/min cm^2 at 850°C under dry conditions. Li et al.[10] observed a H_2 permeation flux of 0.015 mL/min cm^2 through a $BaCe_{0.9}Mn_{0.1}O_{3-\delta}$ membrane at 900°C, and that the H_2 permeation flux of a $BaCe_{0.95}Nd_{0.05}O_{3-\delta}$ (BCN)[11] membrane was only 0.026 mL/min cm^2 at 925°C when fed with a wet mixture of 80% H_2 in He. Moreover, Wei et al.[12] observed a H_2 permeation flux of 0.026 mL/min cm^2 when a mixture of 80% H_2 in He was used as the feed gas at 900°C

Correspondence concerning this article should be addressed to H. H. Wang at hhwang@scut.edu.cn.

Table 1. Properties of the Membranes Based on Perovskite-Type Mixed Proton-Electron Compounds

Membrane Material	T (°C)	Membrane Geometry	Thickness (mm)	Feed Gas	J_{H_2} (mL/min cm^2)	CO_2 Stability	Reference
$SrCe_{0.95}Eu_{0.05}O_{3-\delta}$	850	Disk	1.72	100%H_2	0.0043	–	9
$BaCe_{0.9}Mn_{0.1}O_{3-\delta}$	900	Disk	1.64	H_2/N_2	0.015	–	10
$BaCe_{0.95}Nd_{0.05}O_{3-\delta}$	925	Disk	0.7	Wet 80%H_2/He	0.026	–	11
$SrCe_{0.95}Tb_{0.05}O_{3-\delta}$	900	Disk	1.0	80%H_2/He	0.026	–	12
$SrCe_{0.95}Yb_{0.05}O_{3-\alpha}$	950	Hollow-fiber	<250 μm	35.9%H_2/Ar	0.20	–	13
Ni-$BaCe_{0.95}Tb_{0.05}O_{3-\delta}$	850	Disk	90 μm	50%H_2/N_2	0.914	–	14
$BaCe_{0.9}Gd_{0.1}O_3$	>600	–	–	–	–	Low	18
Ni-$BaCe_{0.8}Y_{0.2}O_3$	900	Disk	0.75	30%CO_2/40% H_2/He	≈0	Low	19
$BaCe_{0.9}Y_{0.1}O_{2.95}$	850–1000	–	–	–	–	Low	20
$Ba(Zr_{0.5}Ce_{0.3}Y_{0.2})O_{2.9}$	>550	–	–	–	–	Low	21
$BaCe_{0.85-x}Zr_xSm_{0.15}O_{3-\delta}$ $(0<x<0.2)$	500−900	–	–	–	–	Low	22

with a $SrCe_{0.95}Tb_{0.05}O_{3-\delta}$ membrane. These studies showed that the known single perovskite membranes exhibited very low H_2 permeation fluxes (<0.03 mL/min cm^2).

Intensive efforts have been made by many researchers to improve the H_2 permeation flux through perovskite-type membranes to develop innovative membrane geometries without using new materials. One approach considers a hollow-fiber configuration with thinner walls. Another design utilizes a membrane with an asymmetric wall structure. For example, the H_2 permeation flux of $SrCe_{0.95}Yb_{0.05}O_{3-\alpha}$ (SCYb) hollow-fiber membranes could reach 0.20 mL/min cm^2 when fed with a mixture of 35.9% H_2 in Ar at 950°C.[13] The hydrogen permeation flux through an asymmetric Ni-$BaCe_{0.95}Tb_{0.05}O_{3-\delta}$ cermet membrane reached 0.914 mL/min cm^2 at 850°C when fed with a 50% H_2 in N_2 mixture.[14] However, pervoskite-type membranes suffer from poor chemical stability under atmosphere containing steam and CO_2 because of the reaction between the alkaline earth metal ions and CO_2.[15,16] For example, Gopalan and Virkar[17] discovered that $SrCeO_3$ and $BaCeO_3$ were thermodynamically unstable with respect to the formation of carbonates in the presence of CO_2. Hyun Ryu and Haile[18] reported that $BaCe_{0.9}Gd_{0.1}O_3$ and $BaCe_{0.9}Nd_{0.1}O_3$ gradually gained weight above 600°C according to thermal gravimetric analysis (TGA) and differential thermal analysis (DTA) curves collected under flowing CO_2, which could be explained by the reaction between CO_2 and the membrane material. Moreover, Zuo et al.[19] found that the H_2 permeation flux through the Ni-$BaCe_{0.8}Y_{0.2}O_3$ (BCY20) cermet membrane sharply decreased when a feed gas with 30% CO_2 was used. The H_2 permeation flux decreased by approximately 53% during the first hour and by approximately 91% after 7 h of operation. In addition, the Y-doped barium cerate $BaCe_{0.9}Y_{0.1}O_{2.95}$ (BCY10) decomposed into $BaCO_3$ and CeO_2 at 850–1000°C under a CO_2 atmosphere.[20] Furthermore, Tu et al.[21] reported that even Zr-doped Ba $(Zr_{0.5}Ce_{0.3}Y_{0.2})$ $O_{2.9}$ and Ba $(Zr_{0.4}Ce_{0.4}Y_{0.2})$ $O_{2.9}$ decomposed to $BaCO_3$ and $Zr_{0.8-x}Ce_xY_{0.2}O_2$ above 550°C under a CO_2 atmosphere. The weight of Sm+Zr-codoped $BaCe_{0.85-x}Zr_xSm_{0.15}O_{3-\delta}$ (BCZS) $(0 < x < 0.2)$ was also reported to increase continuously from 500 to 900°C under pure CO_2 because of the formation of carbonates.[22] These results indicated that the perovskite-type membranes with low Zr-doping or without Zr-doping had poor CO_2 stability due to the formation of carbonates. A summary of the properties of the above perovskite-type membranes is shown in Table 1.

Recently, lanthanum tungstate has received significant attention regarding its use as a new type of mixed proton-electron conducting material.[23–25] Escolástico et al.[26] found that the H_2 permeation flux through a $La_{5.5}WO_{11.25-\delta}$ membrane only changed slightly over 72 h when using a mixture of 15% CO_2 in Ar as a sweep gas at 800°C. Due to the alkaline earth metal-free material of lanthanum tungstate, it should be stable in CO_2-containing atmospheres. Recently, Mo-substituted lanthanum tungstate membranes were studied,[27–29] and were found to exhibit high mixed proton-electron conductivities. Therefore, in this article, Mo-substituted lanthanum tungstate $La_{5.5}W_{0.6}Mo_{0.4}O_{11.25-\delta}$ (LWM04) was developed as a mixed proton-electron conducting membrane material. A membrane with a U-shaped hollow-fiber configuration was adopted because the U-shaped geometry offers several advantages.[30,31] First, the wall thickness of hollow-fiber membranes is thin, resulting in a relatively high H_2 permeation flux. Second, the U-shaped hollow-fiber membrane is easily sealed at high temperatures. Finally, the U-shaped hollow-fiber membranes can withstand variable temperature ranges due to its shrinkable and expandable properties. The chemical stability of U-shaped LWM04 hollow-fiber membranes for H_2 permeation in the presence of CO_2 was systematically investigated.

Experimental

First, $La_{5.5}W_{0.6}Mo_{0.4}O_{11.25-\delta}$ (LWM04) powder was synthesized using solid-state reactions. The appropriate stoichiometric proportions of La_2O_3 (99.9%), WO_3 (99.0%), and MoO_3 (99.5%) were weighed and the mixed oxides were ball milled in acetone for 10 h after they were combined to obtain a homogeneous precursor. Next, the precursor was dried and ground. Finally, the powders were calcined at 900°C

Table 2. Conditions for Preparing of U-Shaped LWM04 Hollow-Fiber Membrane Precursors

Parameter	
Composition of the spinning suspension (wt %)	
LWMO powder	45.65
PESf A-300	10.66
NMP	42.63
PVP K30	1.06
Spinning temperature (°C)	25
Air gap (cm)	1
Spinning pressure (bar)	0.1
Internal coagulant rate (mL/min)	1.5

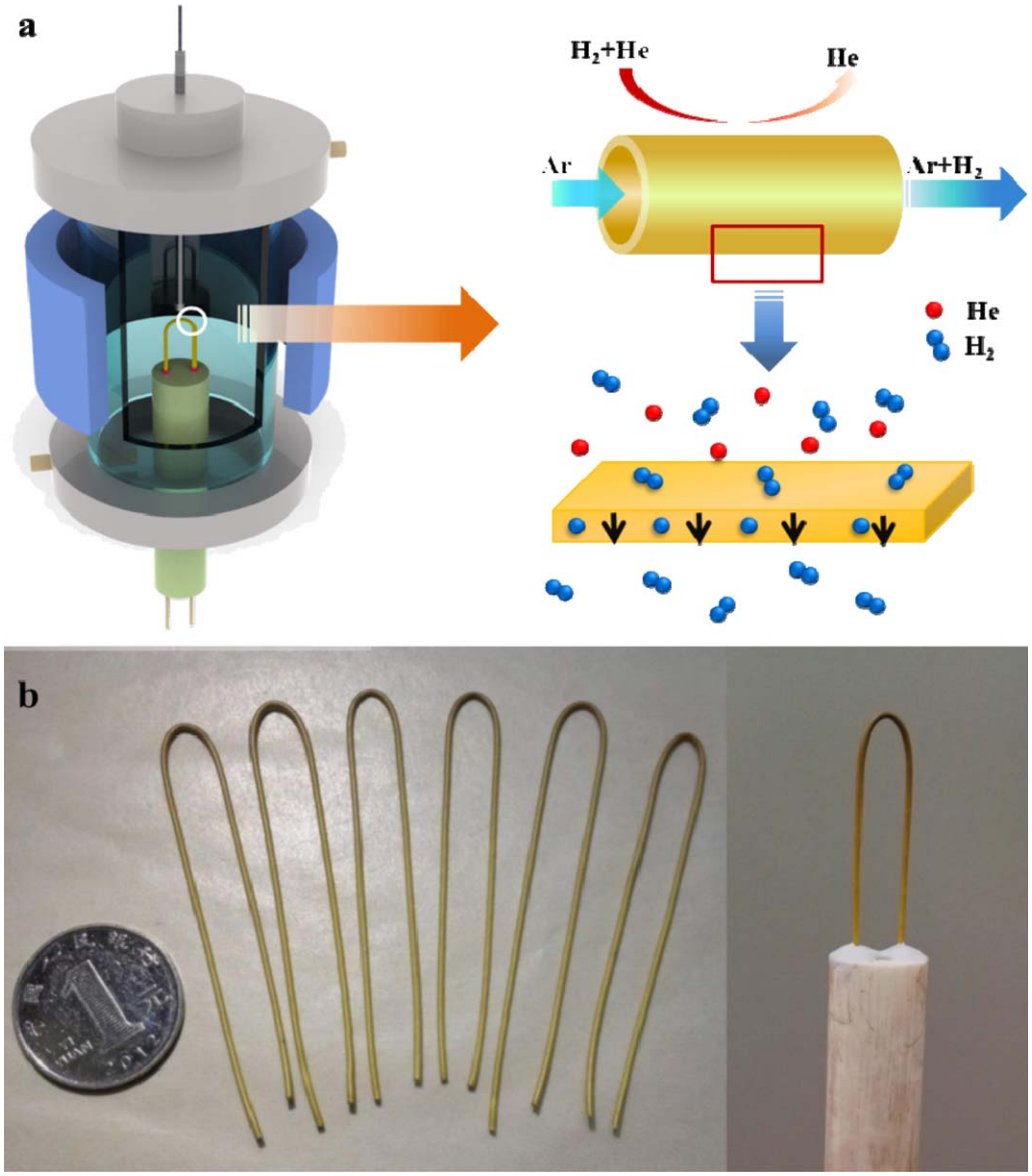

Figure 1. (a) Schematic diagram of the hydrogen permeation apparatus for testing U-shaped hollow-fiber membranes at high temperatures and (b) photos of the U-shaped hollow fiber membranes.

[Color figure can be viewed in the online issue, which is available at wileyonlinelibrary.com.]

for 10 h. Only the powder that passed through a 200-mesh sieve was used for preparing the hollow-fiber membranes.

The U-shaped hollow-fiber membranes were prepared using wet-spinning phase-inversion and sintering. Details regarding the spinning setup and used procedures can be found in our previous publication.[30] Briefly, the starting suspension slurry consisted of 45.65 wt % LWM04 powder, 42.63 wt % *N*-methyl-2-pyrrolidone (NMP) (as the solvent), 10.66 wt % poly-ethersulfone (PESf) (as the polymer binder), and 1.06 wt % polyvinyl pyrrolidone (PVP) (as the additive). Deionized water and tap water were used as internal and external coagulants, respectively. The parameters of the spinning procedure are presented in Table 2. The hollow-fiber precursors were further sintered at 1500°C for 10 h in static air to obtain the final hollow-fiber membranes.

The phase and micro structures of the LWM04 powder and the hollow-fiber membranes were characterized using x-ray diffraction (XRD, Bruker-D8 ADVANCE, and Cu Kα radiation) and scanning electron microscopy (SEM, JEOL JSM-6700F). A thermogravimetric analysis was conducted to study the stability of the LWM04 powder under a pure CO_2 atmosphere. The samples were heated under CO_2 or N_2 atmospheres at a rate of 5°C/min before holding at 800°C for 30 min. The H_2 permeation through the LWM04 hollow-fiber membranes was measured at high temperatures using a home-made apparatus, as shown in Figure 1a. The U-shaped hollow-fiber membrane was sealed over a ceramic tube with two channels using a commercial sealant (2767, Huitian, Hubei, China). Figure 1b shows photos of the U-shaped hollow-fiber membranes. A mixture of He and H_2 was fed into the side of the shell, and the H_2 partial pressure was adjusted by changing the flow rates of He and H_2. Next, Ar was fed through the side of the core as a sweep gas. The flow rates of these gases were controlled using mass flow controllers (Seven Star D08-4F/ZM) and were calibrated using a soap bubble flow meter. The sweep gas and feed gas were

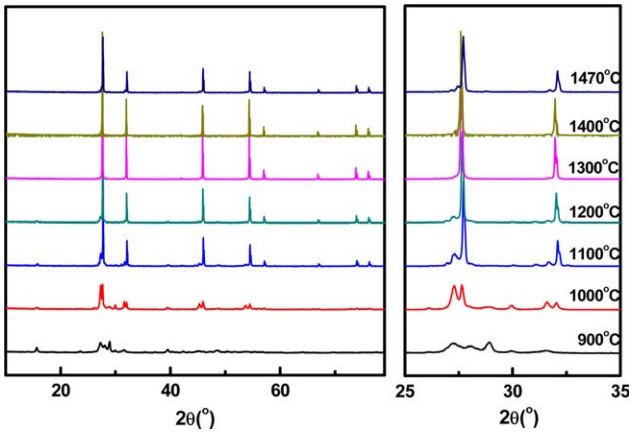

Figure 2. XRD patterns of the LWM04 powder calcined at different temperatures.

[Color figure can be viewed in the online issue, which is available at wileyonlinelibrary.com.]

humidified by achieved deionized water saturation at 28°C. The components of the permeated gases were detected using an online-coupled gas chromatograph (GC, Agilent 7890) that was equipped with a thermal conductivity detector and a zeolite 13X column. The GC was regularly calibrated to ensure that the data were reliable. The leakage from the sealant at high temperatures was less than 5% during all of the measurements. The effective area of the U-shaped hollow-fiber membrane was 1.44 cm^2.

Results and Discussion

The XRD patterns of the powder calcined at different temperatures are shown in Figure 2. A single phase was not achieved until the calcination temperature exceeded 1300°C. At 1300°C, the solid-state reactions among the three oxides proceeded to completion to form a complex cubic fluorite structure, as described in the literature.[29] A new La_6MoO_{12} phase was formed when the sintering temperature was greater than 1400°C, which may be attributed to the relatively higher Mo content in LWM04.[29]

A thermogravimetric analysis was performed to determine the stability of LWM04 under a CO_2 atmosphere at high temperatures. For comparison, $BaCe_{0.95}Tb_{0.05}O_{3-\delta}$ (BCTb), an alkaline earth metal-containing proton-electron conducting material with a perovskite-type structure, was investigated under the same conditions. Figure 3a shows the thermogravimetric curves of LWM04 and BCTb under pure CO_2 and N_2 atmospheres between room temperature and 800°C. The mass of the LWM04 powder slightly decreased under the pure CO_2 atmosphere as the temperature increased, and a similar trend was observed for the N_2 treatment. The slight weight loss potentially resulted from dehydration and the release of oxygen from the LWM04.[32] By contrast, the weight of the perovskite-type BCTb sharply increased when the temperature exceeded 400°C under the CO_2 atmosphere. The weight of BCTb slightly decreased under the N_2 atmosphere due to the release of oxygen. After the thermogravimetric assays, the phase structures of the samples were investigated using XRD, as shown in Figure 3b. The phase structure of the LWM04 powder treated under the CO_2 atmosphere was identical to those of the N_2-treated and fresh LWM04 powders. This result indicated that the samples maintained their fluorite structure and that no carbonate was formed. As shown in Figure 3b, the perovskite structure of BCTb decomposed to form $BaCO_3$ and CeO_2 after the CO_2 treatment. The increasing BCTb weight resulted from the formation of carbonates. These results revealed that LWM04 exhibits excellent structural stability under CO_2-containing atmospheres relative to alkaline earth metal-containing perovskite oxides.

To understand the phase structure evolution better during the heating and cooling processes in different atmospheres, the *in situ* XRD patterns of LWM04 powder under a CO_2 atmosphere at 30–1000°C are shown in Figure 4a. No carbonate peaks appeared from 30 to 1000°C, indicating that the LWM04 powder showed excellent stability under CO_2. The *in situ* XRD patterns of the LWM04 powder in air and N_2 at 30–1000°C are shown in Figures 4b, c and indicate that the phase structure of the LWM04 powder remained unchanged during the heating and cooling processes. Figure 5 shows the XRD patterns of the LWM04 powders that were treated with CO_2 and 8% H_2/Ar at 900°C for 15 and 5 h, respectively. No phase changes were observed in the XRD patterns obtained from the samples after treatment, indicating the good phase and chemical stabilities of LWM04 under CO_2 and low concentrations of H_2.

Figure 6 shows the SEM images of the LWM04 hollow-fiber membranes that were sintered at 1500°C. As shown in

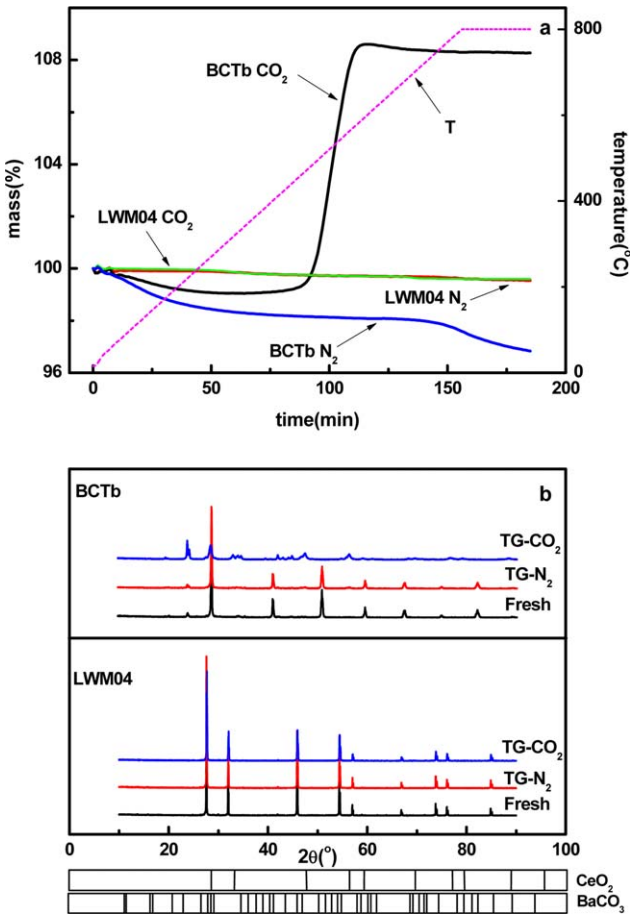

Figure 3. (a) Thermogravimetric curves of the LWM04 and $BaCe_{0.95}Tb_{0.05}O_{3-\delta}$ powders under N_2 and CO_2 atmosphere between room temperature and 800°C and (b) XRD patterns of the samples after thermogravimetric measurement.

[Color figure can be viewed in the online issue, which is available at wileyonlinelibrary.com.]

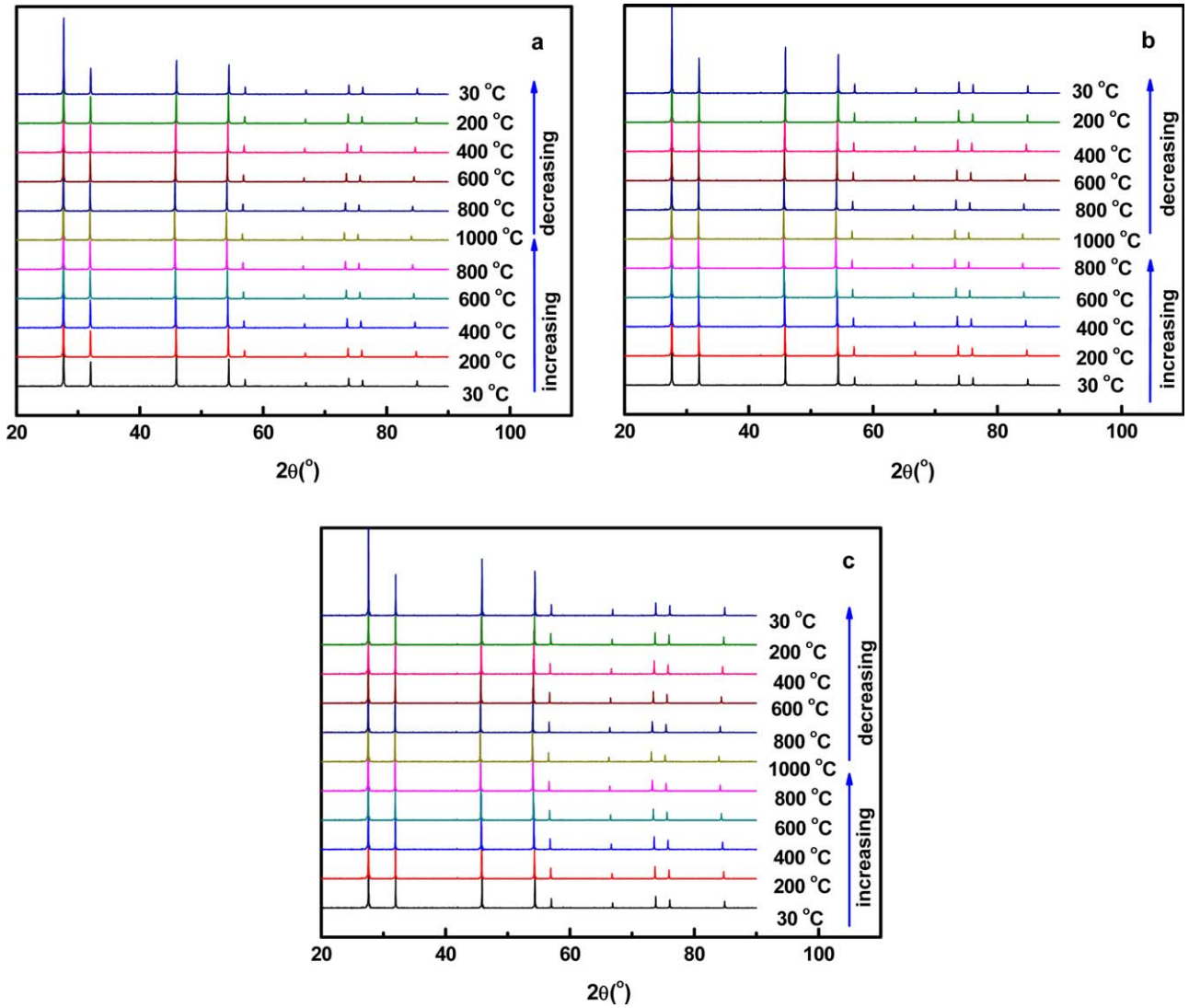

Figure 4. *In situ* XRD patterns of the LWM04 powder in (a) CO_2, (b) air, and (c) N_2 atmospheres after changing the temperature from 30 to 1000°C and back to 30°C. Heating rate: 12°C/min, equilibration time at each temperature: 30 min for recording the XRD data.

[Color figure can be viewed in the online issue, which is available at wileyonlinelibrary.com.]

Figures 6a, b, the cross-section of the hollow-fiber membrane consisted of two finger-like structures near the inner and outer surfaces and a sponge-like structure in the middle. All cavities were closed to the surroundings (i.e., "closed porosity"). These close cavities have no beneficial effect on both of the bulk diffusion and surface exchange processes. They only act as a support for the dense layer in the hollow fiber membrane structure, which enhances the mechanical strength of the hollow fiber. The wall thickness of the membrane was approximately 200 μm. No major defects were observed in the SEM images of the inner and outer membrane surfaces (as shown in Figures 6c, d).

Figure 7 presents the H_2 permeation flux through the hollow-fiber membrane as a function of temperature. The H_2 permeation flux increased approximately linearly as the temperature increased from 700 to 975°C. The presence of steam on the sweep and feed sides of the membrane significantly affected the H_2 permeation flux. As shown in Figure 7, when the feed side was humidified (condition 2), the H_2 permeation flux reached 0.54 mL/min cm^2 at 975°C, this flux value was slightly higher than that value observed under dry conditions (condition 1), which was due to the hydration of the membrane. The surface reaction mechanism is shown in Figure 8b.

When the sweep side was humidified (condition 3 in Figure 7), the H_2 permeation flux reached a maximum of 1.36 mL/min cm^2 at 975°C. Two reasons account for this relatively high H_2 production rate. First, the presence of steam on the sweep side resulted in the formation of additional protons. The reaction of water with oxygen vacancies or lattice oxygen produces two protonated oxygen atoms.[11] The hydrogen permeation flux of mixed proton-electron conducting membranes can be calculated using Wagner transport theory. If the diffusion of protons is a rate limiting step, the Wagner equation can be written as follows

$$J_{H_2} = \frac{RT}{4F^2L} \int_{P'_{H_2}}^{P''_{H_2}} \frac{\sigma_{OH^\bullet}(\sigma_{e'} + \sigma_{h^\bullet})}{\sigma_t} d\ln P_{H_2} \quad (1)$$

where J_{H_2} is the hydrogen permeation flux, R is the ideal gases constant, F is the Faraday constant, L is the thickness

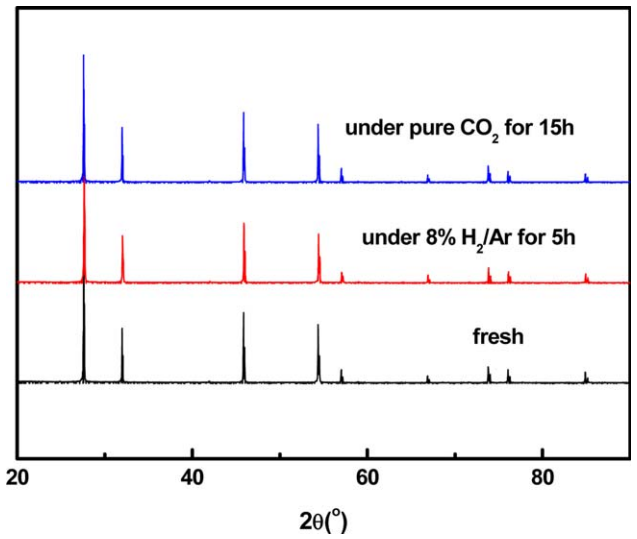

Figure 5. XRD patterns of the LWM04 powders treated with pure CO_2 and 8% H_2 in Ar at 900°C for 15 and 5 h, respectively.

[Color figure can be viewed in the online issue, which is available at wileyonlinelibrary.com.]

of the membrane, σ_i is the conductivity of species i, and the subscripts $OH^{\bullet}$, e', $h^{\bullet}$, and t denote the proton, electron, electron hole, and total conductivity, respectively. In addition, P''_{H_2} and P'_{H_2} represent the partial pressures of hydrogen in the feed and sweep sides, respectively.

According to the Wagner equation (Eq. 1), the proton conductivity of the membrane has important effects on the hydrogen permeation flux. When the membrane was tested under dry conditions, molecular hydrogen reacted with lattice oxygen to generate protonated lattice oxygen, and liberated electrons on the membrane surface according to Eq. 2[11]

$$H_2 + 2O_o^x \rightarrow 2OH_o^{\bullet} + 2e' \quad (2)$$

where, O_o^x is the lattice oxygen and $OH_o^{\bullet}$ is the protonated lattice oxygen. When steam was introduced on the membrane surface, additional protons were formed as follows according to Eq. 3[11]

$$H_2O + V_o^{\bullet\bullet} + O_o^x \rightarrow 2OH_o^{\bullet} \quad (3)$$

where $V_o^{\bullet\bullet}$ is the oxygen vacancy. According to Eqs. 2 and 3, the existence of steam on the membrane surface results in increasing proton concentrations, increasing the proton conductivity of the membrane. The surface reaction mechanism is shown in Figures 8a, c.

Second, the high H_2 production rate can be attributed to a portion of the detected hydrogen on the sweep side that originates from water splitting.[26] Mixed proton-electron conducting ceramic materials conduct oxygen at high temperatures. Thus, water splitting could occur due to the diffusion of O_2 from higher P''_{O_2} (sweep side) to lower P'_{O_2} (feed side) across

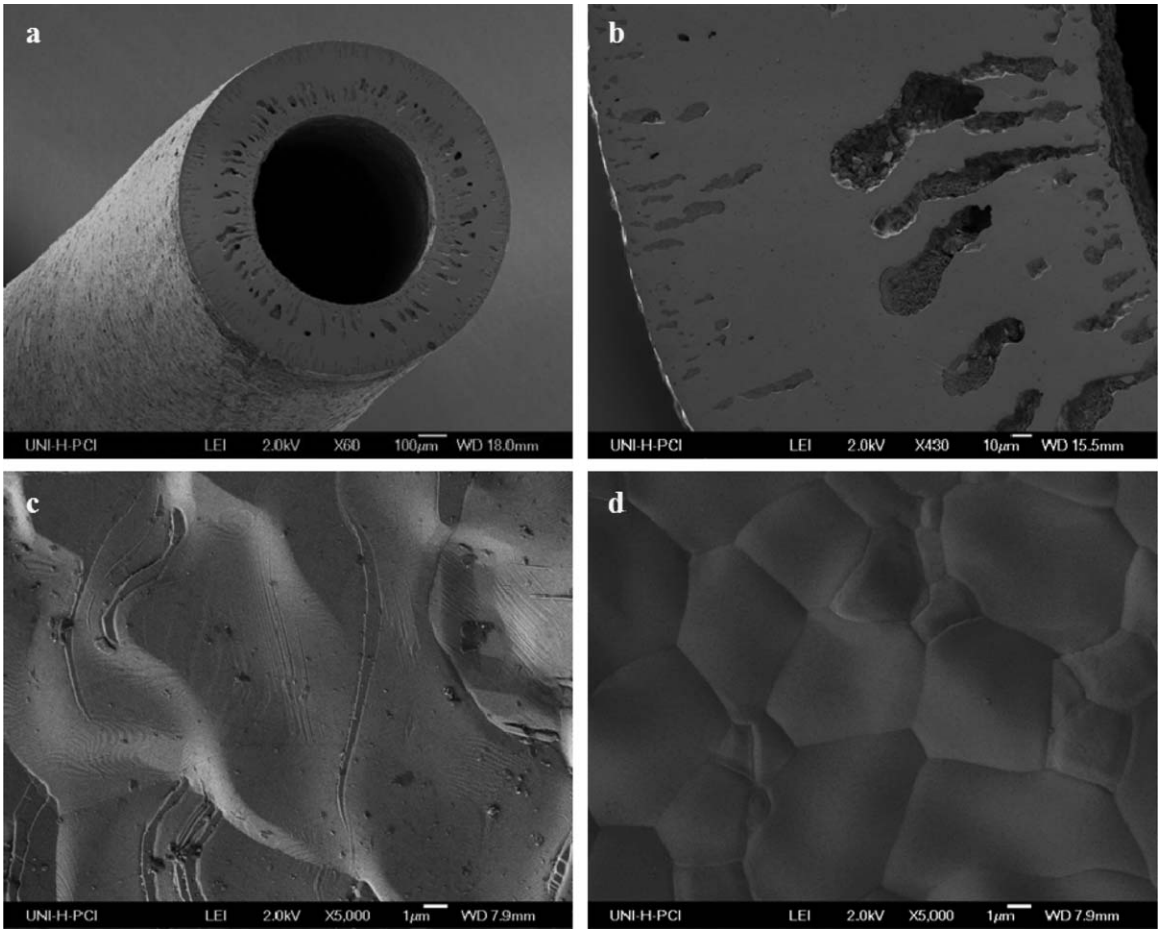

Figure 6. SEM micrographs of fresh LWM04 hollow-fiber membranes: (a) whole image, (b) cross-section, (c) outer surface, and (d) inner surface.

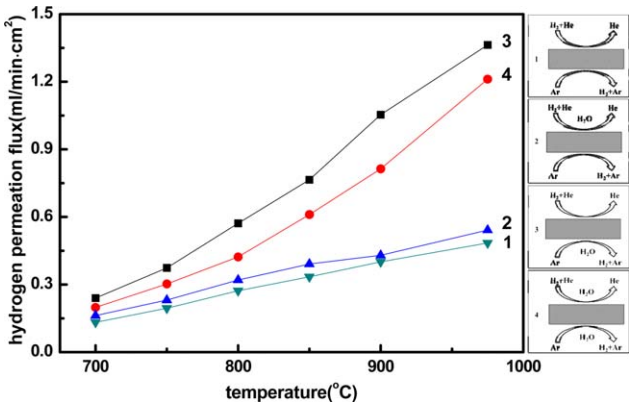

Figure 7. Hydrogen permeation flux through hollow-fiber membranes as a function of temperature for four conditions:(1) dry, (2) steam added to the feed gas, (3) steam added to the sweep gas, and (4) steam added to the sweep gas and the feed gas simultaneously. Conditions: $F_{Ar} = 100$ mL/min, $F_{H2+He} = 80$ mL/min, feed composition 80% H_2 in 20% He.

[Color figure can be viewed in the online issue, which is available at wileyonlinelibrary.com.]

the O_2 partial pressure gradient. However, protons diffuse in the opposite direction, from higher P''_{H_2} (feed side) to lower P'_{H_2} (sweep side). In both cases, the movement of the protons and oxygen ions are balanced by electrons. The oxygen partial pressures on the feed and sweep sides under this condition were calculated and are shown in Table 3. As shown in Table 3, the oxygen partial pressure gradient is the highest under these conditions. Figure 8c shows the hydrogen permeation mechanism under this condition. Similar results were also reported in other studies. Cai et al.[11] found that the H_2 permeation flux through the $BaCe_{0.95}Nd_{0.05}O_{3-\delta}$ membrane reached 0.026 mL/min cm^2 when the steam concentration of in the feed gas was 15 vol %, which was much higher than that under dry conditions. In addition, the total conductivities of $La_2Ce_2O_7$[33] and $La_{28-y}(W_{1-x}Mo_x)_{4+y}O_{54+\delta}$ $-_y(W_{1-x}Mo_x)_{4+y}O_{54+\delta}$ $(x = 0\_1,\ y = 0.923)$[29] significantly increased when steam was added.

The H_2 permeation flux reached 1.21 mL/min cm^2 when steam was added to the sweep and feed gases (condition 4). This flux value was slightly lower than that value observed under conditions where only the sweep gas was humidified. In this case, the slight decrease in the H_2 permeation flux potentially resulted from the lower O_2 partial pressure gradient between the two sides of the membrane. As shown in Table 3, the O_2 partial pressure gradient under condition 4

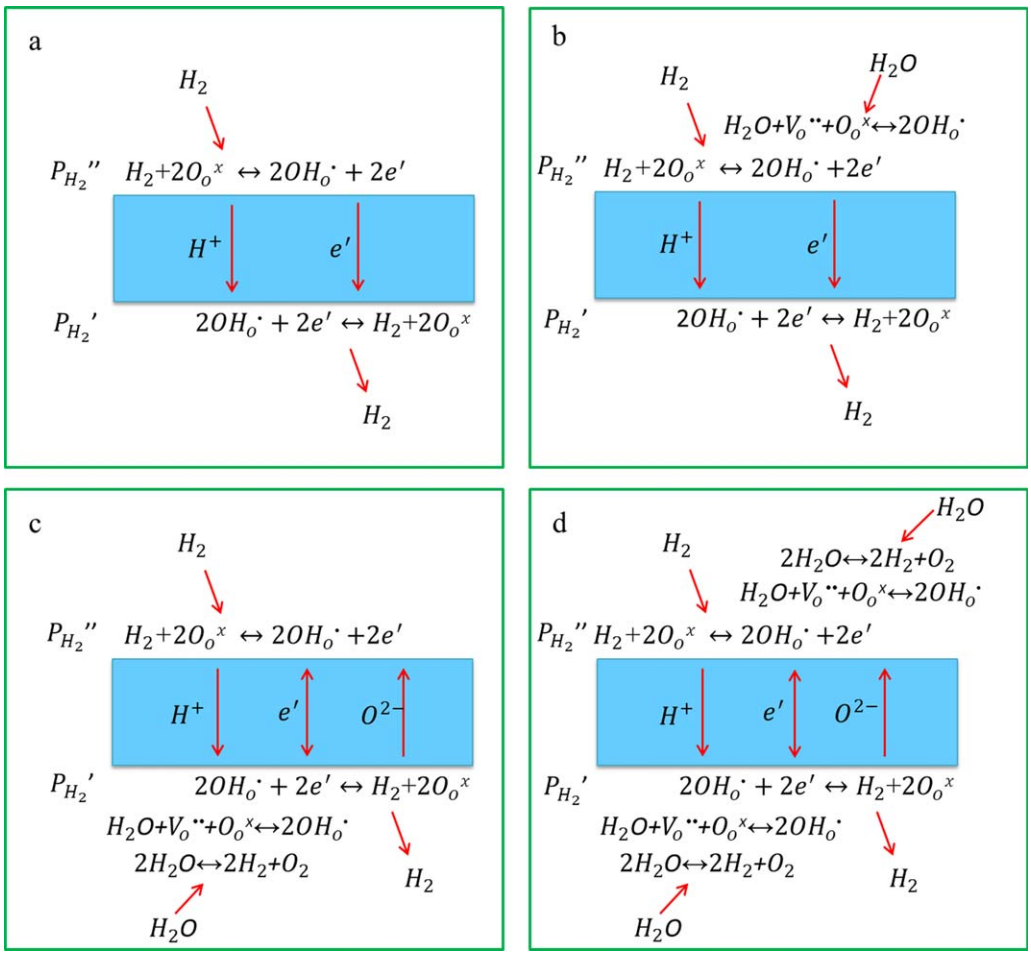

Figure 8. Surface reaction mechanism when steam is introduced on the membrane surface: (a) dry, (b) steam only added to the feed gas, (c) steam only added to the sweep gas, and (d) steam added to the sweep gas and the feed gas simultaneously.

[Color figure can be viewed in the online issue, which is available at wileyonlinelibrary.com.]

Table 3. Calculated Oxygen Partial Pressures for the Three Conditions in the Hydrogen Permeation Measurements.

	Feed Side is Humidified (Condition 2)		Sweep Side is Humidified (Condition 3)		Both Sides are Humidified (Condition 4)	
T (°C)	P'_{O_2}(atm) (Feed Side)	P''_{O_2}(atm) (Sweep Side)	P'_{O_2}(atm) (Feed Side)	P''_{O_2}(atm) (Sweep Side)	P'_{O_2}(atm) (Feed Side)	P''_{O_2}(atm) (Sweep Side)
975	2.15 E −18	3.50 E −18	3.86 E −26	3.64 E −11	2.15 E −18	4.14 E −11
900	1.00 E −19	2.49 E −19	1.81 E −27	2.78 E −12	1.008 E −19	4.418 E −12
850	1.04 E −20	3.12 E −20	1.88 E −28	5.128 E −13	1.048 E −20	7.668 E −13
800	8.79 E −22	3.68 E −21	1.58 E −29	7.87 E −14	8.79 E −22	1.249 E −13
750	5.839 E −23	4.319 E −22	1.05 E −30	1.02 E −14	5.83 E −23	1.50 E −14
700	2.94 E −24	3.87 E −23	5.28 E −32	1.18 E −15	2.94 E −24	1.55 E −15

In these calculations, the experimental P'_{H_2} value was used and it was assumed that $P''_{H_2} = 0.8$ atm, $P_{H2O}(\text{wet}) = 0.0373$ atm and $P_{H2O}(\text{dry}) = 5 \times 10^{-6}$ atm.

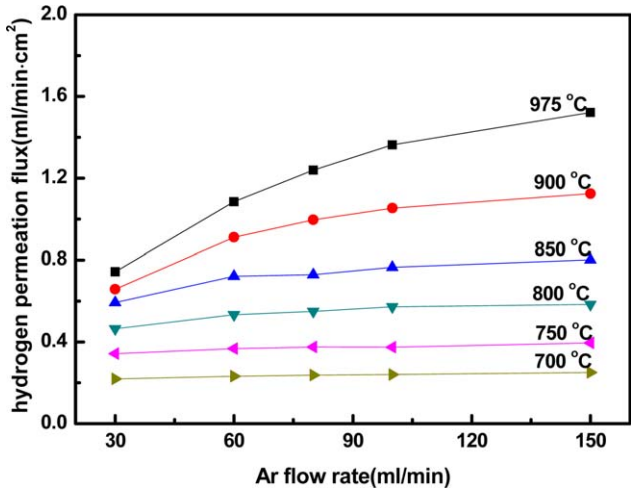

Figure 9. Dependence of the hydrogen permeation flux on the Ar flow rates on the sweep side at different temperatures.

Conditions: $F_{H2+He} = 80$ mL/min, feed composition 80% H_2 in 20% He, humidified Ar as the sweep gas. [Color figure can be viewed in the online issue, which is available at wileyonlinelibrary.com.]

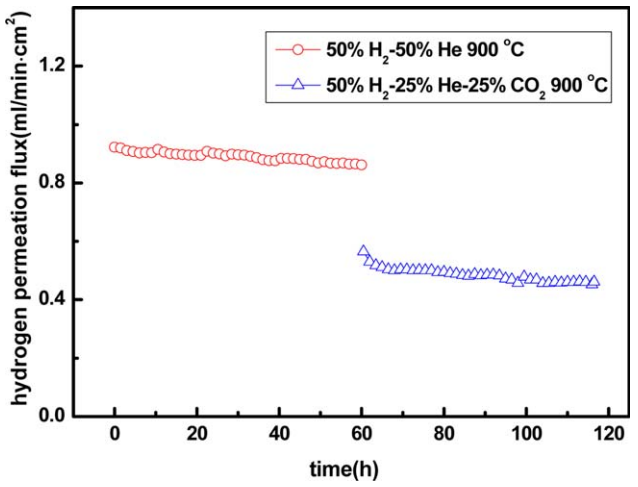

Figure 11. Hydrogen permeation flux as a function of operation time at 900°C.

Conditions: $F_{Ar,humidified} = 100$ mL/min, $F_{H2+He+CO2} = 80$ mL/min. [Color figure can be viewed in the online issue, which is available at wileyonlinelibrary.com.]

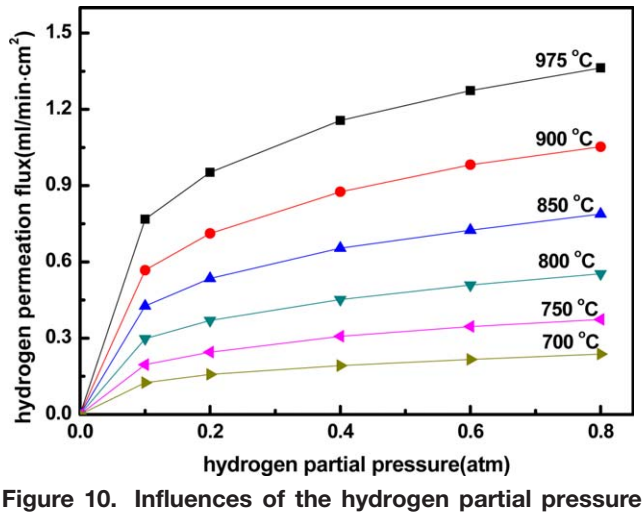

Figure 10. Influences of the hydrogen partial pressure on the feed side on the hydrogen permeation flux. Conditions: $F_{Ar,\ humidified} = 100$ mL/min, $F_{H2+He} = 80$ mL/min.

[Color figure can be viewed in the online issue, which is available at wileyonlinelibrary.com.]

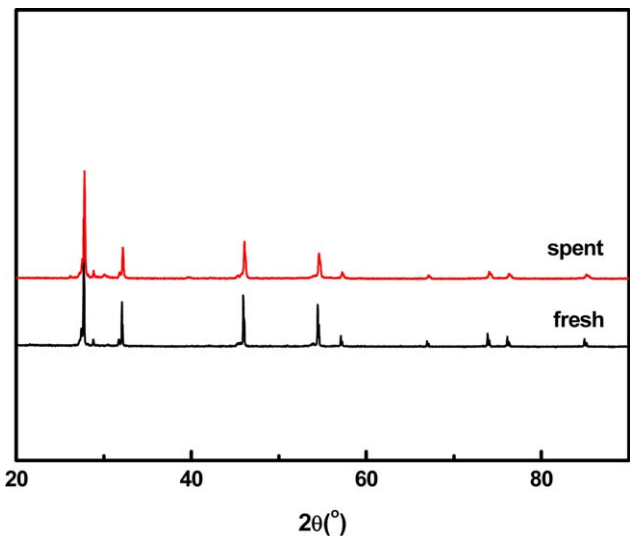

Figure 12. XRD patterns of LWM04 hollow-fiber membranes before and after hydrogen permeation.

[Color figure can be viewed in the online issue, which is available at wileyonlinelibrary.com.]

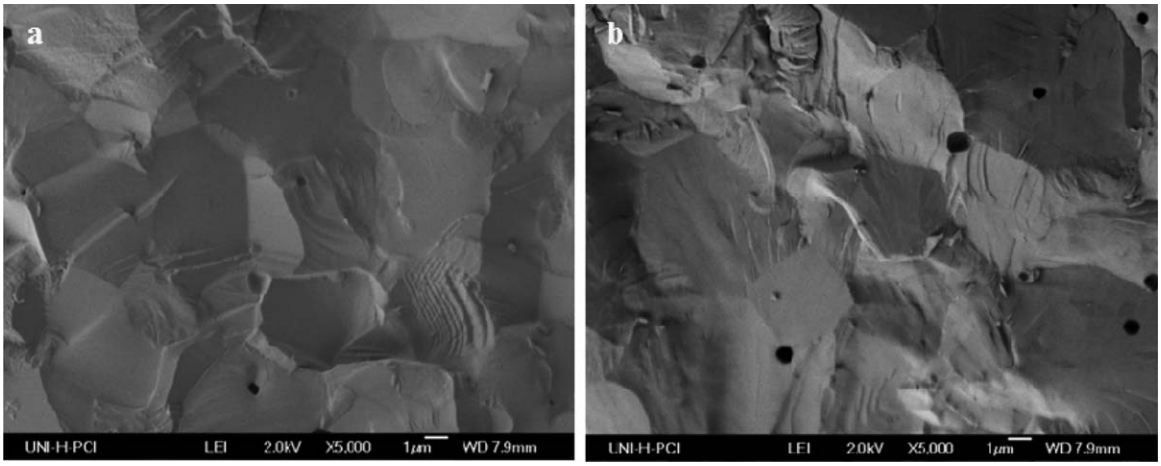

Figure 13. Cross-section of fresh and spent LWM04 hollow-fiber membranes: (a) fresh and (b) spent.

was lower than the O_2 partial pressure gradient under condition 3. Therefore, the amount of O_2 diffusion from the higher P''_{O_2} (sweep side) to the lower P'_{O_2} (feed side) decreased. This decrease suppressed the steam decomposition on the sweep side, decreasing the detected hydrogen. The surface reactions mechanism is shown in Figure 8d.

The dependency of the H_2 permeation flux on the Ar flow rates on the sweep side at different temperatures is shown in Figure 9. A mixture of 80% H_2 and He was used as the feed gas, and humidified Ar was used as the sweep gas. The H_2 permeation flux increased as the Ar flow rates increased on the sweep side. When the Ar flow rate increased, the H_2 partial pressure on the sweep side decreased, increasing of the driving force for H_2 permeation. Additionally, because the proton bulk diffusion and surface exchange rates improved, the H_2 permeation flux increased when the operation temperature increased from 700 to 975°C.

The influence of the feed side H_2 partial pressure on the H_2 permeation flux is presented in Figure 10. The different concentrations of H_2 in the feed gas were adjusted by varying the flow rate of H_2 and He, and the total flow rates of H_2 and He were set to 80 mL/min. As shown in Figure 10, as the H_2 partial pressure on the feed side increased, the H_2 permeation flux increased because the H_2 partial pressure gradient increased across the membrane.

The H_2 permeation flux of the LWM04 hollow-fiber membrane as a function of time was also investigated. As shown in Figure 11, the H_2 permeation flux was maintained at 0.87 mL/min cm^2 for 60 h. A slight decrease was only observed when a mixture of 50% H_2 in He was used as the feed gas. When 25% CO_2 was introduced to the feed side, the H_2 permeation flux initially decreased to 0.50 mL/min cm^2. Next, only a slight further decrease in the H_2 permeation flux was observed. The following three processes may explain the decrease in the H_2 permeation flux. (1) When CO_2 is introduced to the feed side, a fraction of H_2 may react with CO_2 at 975°C to form CO and H_2O.[34] Next, the feed side H_2 partial pressure slightly decreases, reducing the driving force for H_2 permeation and resulting in the observed decrease in the detected H_2 concentration on the sweep side. (2) Steam may be generated on the feed side, and the feed gas may be humidified. The operation condition is that the sweep gas is humidified. According to Figure 7, when steam is added on the sweep and feed sides rather than only the sweep side, the detected hydrogen permeation flux is lower; (3) finally, the lower H_2 permeation flux potentially resulted from the strong adsorption of CO_2 on the LWM04 hollow-fiber membrane surface, resulting in lower H_2 and O_2 surface exchange rates. In addition, similar results have been reported in other studies.[35] For example, Zuo et al.[35] reported that when a feed gas of wet 30% CO_2 (balance 40% H_2/He) was introduced into the feed side, the hydrogen permeation flux of Ni-Ba($Zr_{0.4}Ce_{0.4}Y_{0.2}$)$O_{3-\alpha}$ decreased by approximately 45% during the first hours of exposure. In addition, the slight decrease of the H_2 permeation flux with time could result from the higher Mo contents in the LWM04, which could be reduced more easily than tungsten oxides under the same reducing atmosphere.[36]

Figure 12 presents the XRD patterns of the LWM04 hollow-fiber membranes before and after 120 h of H_2 permeation. The phase structure was maintained after 120 h of H_2 permeation, demonstrating the good phase stability of the LWM04 hollow-fiber membranes under the CO_2-containing atmosphere. The SEM morphologies of the fresh and spent LWM04 hollow-fiber membranes were also compared, as shown in Figure 13. The cross-section of the spent

Table 4. Comparison of Hydrogen Permeation Properties Reported in the Literatures and Those of the LWM04 on Hollow-Fiber Membranes

Membrane Material	T (°C)	Feed Gas	Sweep Gas	J_{H_2} (mL/min cm^2)	CO_2 Stability	Durability	Reference
$SrCe_{0.95}Yb_{0.05}O_{3-\alpha}$	950	35.9% H_2/Ar	Air	0.20	–	–	13
$BaCe_{0.95}Tb_{0.05}O_{3-\alpha}$	1000	50% H_2/He	N_2	0.567	–	–	37
$BaCe_{0.85}Tb_{0.05}Co_{0.1}O_{3-\delta}$	1000	50% H_2/He	N_2	0.385	–	–	38
$BaCe_{0.8}Y_{0.2}O_{3-\alpha}$	1050	50% H_2/He	N_2	0.38	–	–	39
$La_{5.5}W_{0.6}Mo_{0.4}O_{11.25-\delta}$	975	50% H_2/He	Wet Ar	0.87	High	120 h	Our work

membrane remained unchanged. In addition, the spent membrane maintained its density after 120 h of H_2 permeation, indicating that the LWM04 hollow-fiber membrane exhibited good chemical stability under the CO_2-containing atmosphere. Finally, the hydrogen permeation properties and stability of the reported hollow-fiber membranes from the literatures and the LWM04 hollow-fiber membrane described in this work are compared in Table 4. The LWM04 hollow-fiber membrane had the best CO_2 stability (Table 4).

Conclusion

In this work, molybdenum-substituted lanthanum tungstate, $La_{5.5}W_{0.6}Mo_{0.4}O_{11.25-\delta}$ (LWM04), U-shaped hollow-fiber membranes were prepared using wet-spinning phase-inversion and sintering. The hydrogen permeation flux of the LWM04 hollow-fiber membrane was 1.36 mL/min cm^2 when humidified Ar was used as the sweep gas at 975°C. The chemical stability of the LWM04 powder under a CO_2 atmosphere was studied using *in situ* XRD, XRD, and thermogravimetry (TG) measurements. These results revealed that the LWM04 oxides possessed excellent stability under the CO_2 atmosphere. In addition, the hydrogen permeation flux was mostly stable during a 70 h hydrogen permeation test when 25% CO_2 was added to the feed gas, indicating that the LWM04 hollow-fiber membrane was stable in a CO_2 containing atmosphere. According to these results, we concluded that the LWM04 membrane shows excellent stability under CO_2-containing atmospheres. Although a slight decrease of the H_2 permeation flux with time was observed, likely due to the large Mo content in the LWM04, the LWM04 membrane could be applied for industrial separation of hydrogen at high temperatures.

Acknowledgment

The authors greatly acknowledge the financial support provided by the National Science Fund for Distinguished Young Scholars of China (No. 21225625), the Natural Science Foundation of China (No. 21176087), and the Sino-German Center for Science Promotion (GZ 911).

Literature Cited

1. Momirlan M, Veziroglu TN. Current status of hydrogen energy. *Renew Sustain Energy Rev*. 2002;6:141–179.
2. Momirlan M, Veziroglu TN. The properties of hydrogen as fuel tomorrow in sustainable energy system for a cleaner planet. *Int J Hydrogen Energy*. 2005;30:795–802.
3. Li A, Liang W, Hughes R. Fabrication of dense palladium composite membranes for hydrogen separation. *Catal Today*. 2000;56:45–51.
4. Hou K, Hughes R. Preparation of thin and highly stable Pd/Ag composite membranes and simulative analysis of transfer resistance for hydrogen separation. *J Membr Sci*. 2003;214:43–45.
5. Ciavarella P, Moueddeb S, Miachon S, Fiatty K, Dalmon J-A. Experimental study and numerical simulation of hydrogen/isobutane permeation and separation using MFI-zeolite membrane reactor. *Catal Today*. 2000;56:253–264.
6. Dong J, Lin YS, Liu W. Multicomponent hydrogen/hydrocarbon separation by MFI-type zeolite membranes. *AIChE J*. 2000;46:1957–1966.
7. Shi Z, Sun WP, Wang ZT, Qian J, Liu W. Samarium and Yttrium codoped $BaCeO_3$ proton conductor with improved sinterability and higher electrical conductivity. *ACS Appl Mater Interfaces*. 2014;6:5175–5182.
8. Li JL, Yoon H, Keun Oh T, Wachsman ED. High temperature $SrCe_{0.9}Eu_{0.1}O_{3-\delta}$ proton conducting membrane reactor for H_2 production using the water-gas shift reaction. *Appl Catal B Environ*. 2009;92:234–239.
9. Song SJ, Wachsman ED, Rhodes J, Dorris SE, Balachandran U. Hydrogen permeability of $SrCe_{(1-x)}M_xO_{(3-\delta)}$ (x=0.05, M=Eu, Sm). *Solid State Ionics*. 2004;167:99–105.
10. Li GT, Xiong GX, Sheng SS, Yang WS. Hydrogen permeation properties of perovskite-type $BaCe_{0.9}Mn_{0.1}O_{3-\delta}$ dense ceramic membrane. *Chin Chem Lett*. 2001;12:937–940.
11. Cai MY, Liu S, Efimov K, Caro J, Feldhoff A, Wang HH. Preparation and hydrogen permeation of $BaCe_{0.95}Nd_{0.05}O_{3-\delta}$ membranes. *J Membr Sci*. 2009;343:90–96.
12. Wei XT, Kniep J, Lin YS. Hydrogen permeation through terbium doped strontium cerate membranes enabled by presence of reducing gas in the downstream. *J Membr Sci*. 2009;345:201–206.
13. Liu YT, Tan XY, Li K. $SrCe_{0.95}Yb_{0.05}O_{3-\alpha}$ (SCYb) hollow fibre membrane: preparation, characterization and performance. *J Membr Sci*. 2006;283:380–385.
14. Meng XX, Song J, Yang NT, Meng B, Tan XY, Ma ZF, Li K. Ni-$BaCe_{0.95}Tb_{0.05}O_{3-\delta}$ cermet membranes for hydrogen permeation. *J Membr Sci*. 2012;401–402:300–305.
15. Efimov K, Klande T, Juditzki N, Feldhoff A. Ca-containing CO_2-tolerant perovskite materials for oxygen separation. *J Membr Sci*. 2012;389:205–215.
16. Feldhoff A, Arnold M, Martynczuk J, Gesing TM, Wang HH. The sol-gel synthesis of perovskites by an EDTA/citrate complexing method involves nanoscale solid state reactions. *Solid State Sci*. 2008;10:689–701.
17. Gopalan S, Virkar AV. Thermodynamic stabilities of $SrCeO_3$ and $BaCeO_3$ using a molten salt method and galvanic cells. *J Electrochem Soc*. 1993;140(4):1060–1065.
18. Hyun Ryu K, Haile SM. Chemical stability and proton conductivity of doped $BaCeO_3$-$BaZrO_3$ solid solutions. *Solid State Ionics*. 1999;125:355–367.
19. Zuo CD, Lee TH, Song S-J, Chen L, Dorris SE, Balachandran U, Liu ML. Hydrogen permeation and chemical stability of cermet [Ni-$Ba(Zr_{0.8-x}Ce_xY_{0.2})O_3$] membranes. *Electrochem Solid State Lett*. 2005;8(12):J35–J37.
20. Zakowsky N, Williamson S, Irvine JTS. Elaboration of CO_2 tolerance limits of $BaCe_{0.9}Y_{0.1}O_{3-\delta}$ electrolytes for fuel cells and other applications. *Solid State Ionics*. 2005;176:3019–3026.
21. Tu CS, Chien RR, Schmidt VH, Lee SC, Huang CC, Tsai CL. Thermal stability of $Ba(Zr_{0.8-x}Ce_xY_{0.2})O_{2.9}$ ceramics in carbon dioxide. *J Appl Phys*. 2009;105(10):103504-1–103504-7.
22. Kannan R, Gill S, Maffei N, Thangadurai V. $BaCe_{0.85-x}Zr_xSm_{0.15}O_{3-\delta}$ (0.01<x<0.3) (BCZS): effect of Zr content in BCZS on chemical stability in CO_2 and H_2O vapor, and proton conductivity. *J Electrochem Soc*. 2013;160(1):F18–F26.
23. Magraso A, Polfus JM, Frontera C, Canales-Vazquez J, Kalland L-E, Hervoches CH, Erdal S, Hancke R, Saiful Islam M, Norbya T, Haugsrud R. Complete structural model for lanthanum tungstate: a chemically stable high temperature proton conductor by means of intrinsic defects. *J Mater Chem*. 2012;22:1762–1764.
24. Escolástico S, Somacescu S, Serra JM. Solid state transport and hydrogen permeation in the system $Nd_{5.5}W_{1-x}Re_xO_{11.25-\delta}$. *Chem Mater*. 2014;26:982–992.
25. Zayas-Rey MJ, dos Santos-Gómez L, Marrero-López D, Leoń-Reina L, Canales-Vázquez J, Aranda MAG, Losilla ER. Structural and conducting features of niobium-doped lanthanum tungstate, $La_{27}(W_{1-x}Nb_x)_5O_{55.55-\delta}$. *Chem Mater*. 2013;25:448–456.
26. Escolástico S, Solís C, Scherb T, Schumacher G, Serra JM. Hydrogen separation in $La_{5.5}WO_{11.25-\delta}$ membranes. *J Membr Sci*. 2013;444:276–284.
27. Vøllestad E, Vigen CK, Magrasó A, Haugsrud R. Hydrogen permeation characteristics of $La_{27}Mo_{1.5}W_{3.5}O_{55.5}$. *J Membr Sci*. 2014;461:81–88.
28. Escolastico S, Seeger J, Roitsch S, Ivanova M, Meulenberg WA, Serra JM. Enhanced H_2 separation through mixed proton-electron conducting membranes based on $La_{5.5}W_{0.8}M_{0.2}O_{11.25-\delta}$. *ChemSusChem*. 2013;6:1523–1532.
29. Amsif M, Magraso´ A, Marrero-López D, Ruiz-Morales JC, Canales-Vázquez J, Nuñez P. Mo-substituted lanthanum tungstate $La_{28-y}W_{4+y}O_{54+\delta}$: a competitive mixed electron-proton conductor for gas separation membrane applications. *Chem Mater*. 2012;24:3868–3877.
30. Wei YY, Liu HF, Xue J, Li Z, Wang HH. Preparation and oxygen permeation of U-shaped Perovskite hollow-fiber membranes. *AIChE J*. 2011;57(4):975–984.
31. Wei YY, Tang J, Zhou LY, Xue J, Li Z, Wang HH. Oxygen separation through U-shaped hollow fiber membrane using pure CO_2 as sweep gas. *AIChE J*. 2012;58(9):2856–2864.

32. Ivanova ME, Seeger J, Serra JM, Solis C, Meulenberg WA, Fischer W, Roitsch S, Buchkremer HP. Influence of the $La_6W_2O_{15}$ phase on the properties and integrity of $La_{6-x}WO_{12-\delta}$-based membranes. *Chem Mater Res*. 2012;2(1):56–81.
33. Sun W, Fang S, Yan L, Liu W. Investigation on proton conductivity of $La_2Ce_2O_7$ in wet atmosphere: dependence on water vapor partial pressure. *Fuel Cells*. 2012;12(3):457–463.
34. Fang SM, Brinkman K, Chen FL. Unprecedented CO_2-promoted hydrogen permeation in Ni-$BaZr_{0.1}Ce_{0.7}Y_{0.1}Yb_{0.1}O_{3-\delta}$ membrane. *ACS Appl Mater Interfaces*. 2014;6:725–730.
35. Zuo CD, Dorris SE, Balachandran U, Liu ML. Effect of Zr-doping on the chemical stability and hydrogen permeation of the Ni-$BaCe_{0.8}Y_{0.2}O_{3-\alpha}$ mixed protonic-electronic conductor. *Chem Mater*. 2006;18:4647–4650.
36. Marrero-López D, Canales-Vázquez J, Ruiz-Morales JC, Irvine JTS, Núñez P. Electrical conductivity and redox stability of $La_2Mo_{2-x}W_xO_9$ materials. *Electrochim Acta*. 2005;50:4385–4395.
37. Tan XY, Song J, Meng XX, Meng B. Preparation and characterization of $BaCe_{0.95}Tb_{0.05}O_{3-\alpha}$ hollow fibre membranes for hydrogen permeation. *J Eur Ceram Soc*. 2012;32:2351–2357.
38. Song J, Li LP, Tan XY, Li K. $BaCe_{0.85}Tb_{0.05}Co_{0.1}O_{3-\delta}$ perovskite hollow fibre membranes for hydrogen/oxygen permeation. *Int J Hydrogen Energy*. 2013;38:7904–7912.
39. Tan XH, Tan XY, Yang NT, Meng B, Zhang K, Liu SM. High performance $BaCe_{0.8}Y_{0.2}O_{3-\alpha}$ (BCY) hollow fibre membranes for hydrogen permeation. *Ceram Int*. 2014;40:3131–3138.

Manuscript received Sep. 15, 2014, and revision received Feb. 5, 2015.